PHYSICAL REVIEW A VOLUME 22, NUMBER 6 DECEMBER 1980

X-ray spectroscopic diagnosis of laser-produced plasmas, with emphasis on line broadening

J. D. Kilkenny and R. W. Lee
Blackett Laboratory, Imperial College, London, England

M. H. Key and J. G. Lunney
Queen's University, Belfast, Northern Ireland

(Received 19 September 1979; revised manuscript received 15 April 1980)

A detailed account is given of the x-ray spectroscopic diagnosis of plasmas formed by exploding pusher microballoons. The measurements of the electron temperature from the shell and from the core is described. A method for self-consistently fitting all the observed lines of one state of ionization is shown, giving a diagnosis for the electron density and the opacity. Further, it is shown that the self-consistency is only achieved when full line-broadening calculations, taking into account the shifts and asymmetries dependent on the charge of the emitter, are used for the optically thin profiles. It is also shown that non-local-thermodynamic-equilibrium effects are important in the description of the radiation transfer.

I. INTRODUCTION

Space-resolved x-ray spectroscopy has proven to be a powerful diagnostic technique for the study of plasmas produced by laser-driven implosion and compression of gas-filled glass microballoons. When such microballoons are irradiated with a two-beam laser, there are typically two zones of intense x-ray emission. These zones, shown schematically in Fig. 1, are the surface ablation plasma and the core, which consists of compressed gas and glass.

The spectra of these x-ray emitting regions can be used to determine the electron temperature, density and the spectroscopic opacity. A determination of the electron temperature is relatively straightforward. However, there are difficulties in interpreting the line broadening of these plasmas, due to a combination of the high atomic charge of the emitters and the high opacity of the plasma. This paper gives details of our experiments and analyses with particular emphasis on the interpretation of the line broadening.

Previous work[1-19] has used high-order series members which were presumed to be optically thin to obtain an electron density. This density was then used to obtain an opacity from the measured width of a lower-order series member. Here we extend this procedure by presenting a method that is capable of finding whether a whole line series can be fitted consistently or, as is the case, additional line-broadening mechanisms become important for some series members. The method yields a region of electron density and opacity (directly proportional to ground-state density n_1) for which all the line profiles of a series fit consistently. By quantifying the quality of fits, the confidence limits over which consistent fits can be obtained are derived.

The layout of this paper is as follows. Section II describes the experiment and the data reduction. In Sec. III the spectra are analyzed to determine the electron temperature T_e. In Sec. IV, a discussion is given of the method by which the optically thin theoretical profiles are processed to allow for opacity corrections and then compared with experiment. In Sec. V the experimental line profiles are compared to the theoretical optically thick profiles using a homogeneous slab model. It is found that consistent fits are obtained for all the lines only when the full theory for the line profiles is used. In Sec. VI the assumptions inherent in the analysis of Secs. IV and V are critically examined and other models for the opacity broadening are considered.

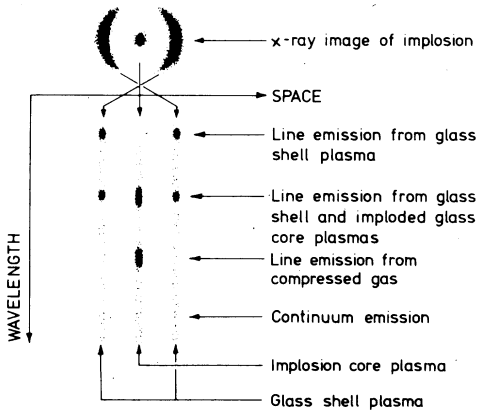

FIG. 1. Schematic of the x-ray emitting regions of laser-compressed microballoons. A typical pinhole image shows surface plasma x-ray emission and compressed core emission. These regions are spatially resolved in one direction by the crystal spectrometer.

II. EXPERIMENTAL DETAILS

The implosion experiments described here were performed using the neodymium glass laser at the Rutherford Laboratory Central Laser Facility. The laser was used in a two-beam mode, each beam giving up to 15 J in 100 ps.[14] The beams were focused on opposite poles of aluminum-coated, gas-filled, glass microballoons which were supported by a 5-μm glass fiber stalk.

The main diagnostics were an x-ray pinhole camera and miniature space-resolving, crystal x-ray spectrometers. The spectrometer was of the type previously described[11] and shown schematically in Fig. 2. The crystal used depended on the spectral range to be recorded. A 5-μm slit lying in the plane of dispersion, which was also normal to the laser beam axis, provided 7-μm spatial resolution parallel to the laser beam axis. A thin foil of either 1.5-μm Al for >8 Å, or 25-μm Be for <8 Å was used as an x-ray filter.

The space-resolved spectra were microdensitometered on a Joyce Lobel Mark 3 densitometer using a numerical aperture of 0.25. The spectra, from the core plasma and the two zones of ablation plasma, were traced separately. The measured neutral density on film was converted to x-ray flux per unit area using the calibration for Kodirex[20] which was the x-ray film used for recording the spectra.

The spectral dispersion was calculated from the interplane spacing of the crystal and the geometry of the spectrometer. To calculate the absolute x-ray emission at a particular wavelength, the integrated reflection coefficient as a function of wavelength must be known. This was measured commercially, using the two-reflection asymmetric method.[21] The half width of the rocking curve was also measured as a function of wavelength. The spatial extent of the core emission was obtained from the space-resolved spectra.

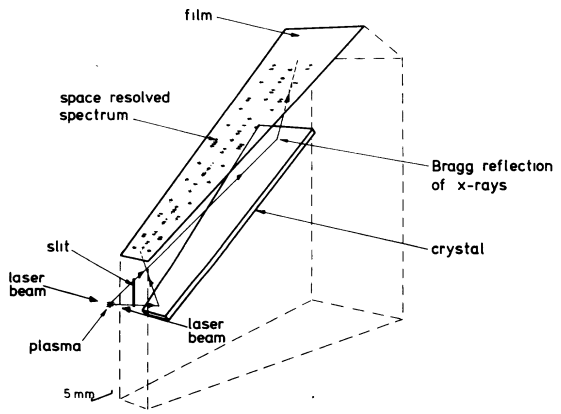

FIG. 2. The miniature space-resolving crystal spectrometer.

The distribution of surface brightness of a uniformly emitting sphere was convolved with the instrument slit width and compared with the spatial extent of the spectra. This procedure defined a sphere of radius R which is the source size. This value of the source size, together with the rocking curve of the crystal determined the spectral resolution of the spectrometer.

III. SPECTROMETRIC DIAGNOSIS USING CONTINUA

A. Electron temperature measured from the continuum

The temperature, density, and dimensions of these plasmas are such that the x-ray continuum emission, at wavelengths less than 10 Å, is optically thin. This continuum emission therefore provides an important diagnostic of the electron temperature T_e.

The continuum-emission spectrum arising from radiative recombination for a plasma of volume V and emitting for a time Δt is given, in J sr^{-1} s, by[22]

$$\epsilon(\nu) = V\Delta t \frac{6.3\times10^{-40} n_e^2}{(kT_e)^{1/2}} \exp\left(-\frac{h\nu}{kT_e}\right) \times \left[\sum_i f_i \left(\frac{X_H}{kT_e}\right)\left(\frac{X_i}{kT_e}\right)\xi_i \exp\left(\frac{X_i}{kT_e}\right)\right], \quad (1)$$

where $f_i = n_i/n_e$ is the number density of ion species "i" relative to n_e the electron number density, X_i is the ionization potential from the ground state of the ion formed by recombination into ion species i, and ξ_i is the degeneracy of the recombined ground state. Note that the Gaunt factors have been set equal to one.

The slope of $\ln\epsilon(\nu)$ is inversely proportional to T_e. Thus the recombination continuum arising from recombination into fully stripped and hydrogenlike aluminum and silicon was used to measure T_e in the ablation plasma, while the continua due to the same ions of neon and silicon were used to calculate T_e from the core plasma.

B. Electron temperature from the state of ionization

Ideally, the relative intensities of hydrogenlike and heliumlike lines can be used to determine T_e. For an ion in a plasma an energy level of principal quantum number n is in local thermodynamic equilibrium (LTE) with respect to higher levels and the continuum of free electrons if[22]

$$n_e > 2\times10^{18} Z^6 T_e^{1/2}/n^{17/2}, \quad (2)$$

n_e given in cm^{-3}. Thus if a plasma is optically thin to the line emission from such a level n of the ion of charge Z, the intensity of the line is pro-

portional to the population density of the next ionization stage $Z+1$. The intensity ratio of the lines arising from high-lying levels of hydrogenlike and heliumlike ions is therefore related to the ratio of the population densities of fully stripped and hydrogenlike ions by

$$\frac{I_H(n,1)}{I_{He}(n',1)} = \frac{A_H(1,n)g_H(n)g_H(1)n_B(1)}{A_{He}(1,n')g_B g_{He}(n')n_H(1)} \times \exp\frac{X_H(n,\infty)-X_{He}(n',\infty)}{kT_e}, \quad (3)$$

where B, H, and H_e indicate the fully stripped, hydrogenlike and heliumlike ions, respectively. Note that since the exponent is small, the temperature dependence is weak.

Therefore, a measurement of $I_H(n,1)$ and $I_{He}(n',1)$ will allow a determination of $n_B(1)$ $n_H(1)$. From Eq. (2) the plasma densities in this study are too low to satisfy LTE to the ground state. Under these conditions the ionization equilibrium is best described by the collisional radiative equilibrium model.[23,24] This model has been used to calculate the ratio $n_B(1)/n_H(1)$ as a function of T_e (with a weak dependence on n_e) using the optically thin calculation.[23] Thus with a measured $n_B(1)/n_H(1)$, T_e can be inferred. The results of calculations with finite optical depths in the Lyman lines[24] indicate an increase in the ionization for a given temperature.

To predict the complete state of ionization of the material, recourse must be made to the simpler coronal model, as the collisional radiative equilibrium (CRE) model has only been calculated for hydrogenlike ions. The fractional populations of other ions was thus taken from the coronal calculations[25] at the temperature that gives the observed ratio $n_B(1)/n_H(1)$. This gives the fraction of atoms which are in the hydrogenic state.

There seems to be an upper limit of 50% for the fraction of atoms which can be in the hydrogenic state of ionization independent of the equilibrium model. This result is approximately the same for both the LTE and coronal models; the other half of the atoms are mainly heliumlike or have bare nuclei.

C. Density measurement from recombination continuum

Equation (1) shows that the intensity of the recombination continuum spectrum $\epsilon(\nu)$ is proportional to $n_e^2 V\Delta t$. Thus if V and Δt are known, n_e can be obtained from $\epsilon(\nu)$, knowing the ionization fraction f_i into which the recombination is taking place. As described earlier, f_i was estimated from the measured temperature and density. The volume V was obtained from an analysis of the space-resolved spectra and the x-ray pinhole camera. The duration of emission of x-rays at 1.0 and 1.4 keV was measured using an x-ray streak camera.[14]

IV. THE PREPARATION AND COMPARISON OF THEORETICAL SPECTRAL PROFILES WITH THE EXPERIMENTAL PROFILES

A. Optically thin profiles

Optically thin profiles were taken from the line-shape calculations of Lee. Details of these calculations are reported elsewhere,[26-28] but a brief description is given here.

Two different sets of optically thin profiles were generated which we refer to as the standard and the full sets of line profiles. For the standard set of profiles the electrons are treated dynamically and the ions are treated as quasistatic perturbers. This treatment is similar to that of Kepple and Griem.[29] For the full set of profiles the ions are treated dynamically, the first-order shift and broadening functions which arise from the charge on the emitter are included, and the fine-structure splitting is included in the calculation for the $L\alpha$ transition.

The main differences in the profiles of the full and the standard calculations are as follows. First, the full calculations provide a somewhat broader profile, which is most noticeable on the α transitions. Second, the full profiles are damped in the central regions of the lines. When Doppler broadening is included the central intensity is decreased and overall the line is wider. This suppression of the central peak is most noticeable for the γ lines. Finally, the full theory predicts small shifts in the line profiles. Numerical examples of these statements are given in Table I.

It is useful to examine the way in which the silicon linewidths of the various transitions depend upon the plasma parameters. Figure 3 shows the full width at half maximum versus electron density for the standard calculation. It should be emphasized that these widths are without any Doppler, opacity, or instrument broadening.

The $L\alpha$ line is relatively narrow. The $L\beta$ line has a characteristic shape with a dip at the line center. The half width measured from the peaks of the profile is well represented by

$$\delta\lambda_{1/2} = 5.5(n_e/10^{22})^{0.57\pm0.03}$$

in the region $10^{22} < n_e < 3\times10^{23}$ cm^{-3}. All $\delta\lambda_{1/2}$ are measured in mÅ.

The L_γ line has a characteristic shape with a very narrow central feature, together with a much wider shoulder. The full half width measured from the peak of the profile is shown, together

TABLE I. Comparison of broadening and shifts for both full and standard theory. Wavelengths are in mÅ. Note the slight narrowing of the $L\beta$ profile with the full theory. This is due to the asymmetry. No Doppler broadening is included.

Spectral line	Si $T_e=5.2\times10^6$ K, $n_e=1.5\times10^{23}$ cm^{-3}				Al $T_e=5.2\times10^6$ K, $n_e=2\times10^{22}$ cm^{-3}			
	$\Delta\lambda_{1/2}$		shift or % asymmetry		$\Delta\lambda_{1/2}$		shift or % asymmetry	
	stand.	full	stand.	full	stand.	full	stand.	full
$L\alpha$	0.62	2.65	0	+0.85	1.2	4.7	0	+0.94
$L\beta$	26.5	24.0	0	10%	13	12	0	12%
$L\gamma$ [a]	56	62	0	+4.5	28	29	0	+2.2
$L\gamma$	8	31	0		1.33	13	0	
$L\delta$	64	63	0	−0.5%	30	31	0	−0.5%

[a] Half width measured from the highest point on shoulder.

with the full half width measured from the highest point on the shoulder. The latter is well represented by

$$\delta\lambda_{1/2}=13(n_e/10^{22})^{0.58\pm0.02}.$$

The full half width of the $L\delta$ line is represented by

$$\delta\lambda_{1/2}=14(n_e/10^{22})^{0.60\pm0.02}.$$

The heliumlike transitions show similar behavior. The $1s^2$-$1s2p$ line is very narrow. The full half width of the $1s^2$-$1s3p$ line is

$$\delta\lambda_{1/2}=5(n_e/10^{22})^{0.64\pm0.04}.$$

For the $1s^2$-$1s4p$ line the two half widths are

$$\delta\lambda_{1/2}=1(n_e/10^{22})^{0.75\pm0.1}$$

for the center and

$$\delta\lambda_{1/2}=14(n_e/10^{22})^{0.60\pm0.04}$$

for the shoulder.

The variation of the half width (without Doppler broadening) with the electron temperature was also empirically examined. At $n_e=1.5\times10^{23}$ cm^{-3} and with T_e equal to 5×10^6 K, the scaling was $\delta\lambda_{1/2}\propto T_e^{0.2}$. The scaling at lower number densities, with more particles in a Debye sphere, will be even weaker. Thus the major variable upon which the width of the optically thin profiles depends is n_e. A large set of standard line profiles was generated for various values of n_e using a T_e of 5.2×10^6 K, for Al and Si as suggested by the experimental observations. For Ne the experimentally observed temperatures are lower and a temperature of 4.6×10^6 K was used. Because of computational cost a limited number of full profiles were calculated.

B. Additional line-broadening processes

Before comparing with experiment, the optically thin profiles were processed (broadened) in the following order. First, the optically thin profiles were Doppler broadened by an amount corresponding to the ion temperature, assuming $T_e=T_i$. The profiles were then corrected for opacity effects according to the simple formula for the intensity emitted from a uniformly emitting and absorbing slab:

$$I_\nu(l,\nu)=B(\nu)\{1-\exp[-\tau(\nu,l)]\}, \quad (4)$$

where $B(\nu)$ is the black-body function and $\tau(\nu,l)$ is the optical depth at frequency ν due to a slab of length l. The optical depth is defined by

$$\tau(\nu,l)=n_1L(\nu)e^2lf_{1j}/4\epsilon_0mc, \quad (5)$$

where f_{1j} is the absorption oscillator strength for

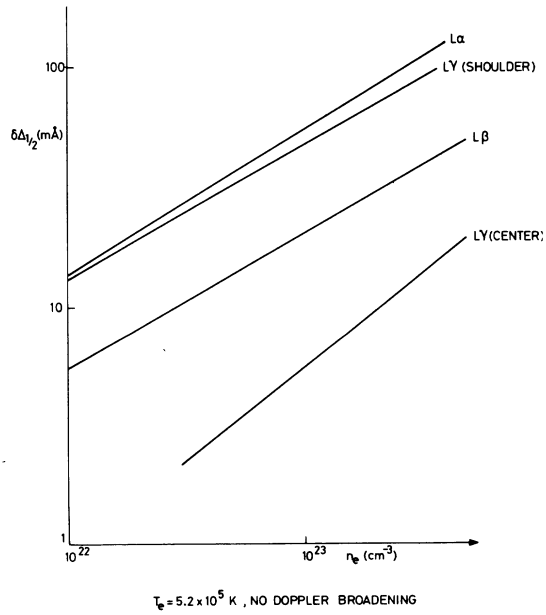

FIG. 3. Theoretical predictions for the FWHM of the Lyman transitions of Si XIV. Doppler broadening is not included.

the transition 1 to j, n_1 is the number density of the lower state of the transition, and $L(\nu)$ is the area-normalized optically thin line profile.

Equation (5) describes the opacity broadening of the intensity emitted normally from a slab in LTE. As the core plasmas of this study are spherical, the opacity broadening from a sphere in the LTE approximation should be calculated. It can be shown that as expected the broadening varies with the optical depth along the line of sight so that

$$I_\nu^s(\nu,\theta)=B(\nu)[1-\exp(-\tau\cos\theta)], \quad (6)$$

where l, in the definition of τ [Eq. (5)], is now the diameter of the sphere and θ is the angle of the ray to the radius of the sphere.

The broadening described by Eqs. (4) and (6) are identical only if $\theta=0$. The θ variation is accounted for by evaluating the flux. This is because if a uniformly emitting sphere is not spatially resolved a detector measures the emitted flux.[30]

The flux from a sphere $F=\int_0^{\pi/2}\cos\theta\, 2\pi\sin\theta I_\nu^s(\nu,\theta)d\theta$ was therefore evaluated for the line profiles and optical depths of the examples in Sec. V. It was found that the spectral intensity emitted from a slab of depth l produced essentially equivalent profiles to the spectral flux emitted from a sphere of diameters $1.5l$ for the $L\alpha$ transition. This is valid for the core $L\alpha$ profiles where it is found that the total optical depth is usually 50 or less.

Finally, the instrument function was convolved with the opacity-corrected profiles. This convolution was performed, assuming a Gaussian instrument profile, with the appropriate half width.

C. Fitting the theoretical profiles to experimental profiles

The theoretical profiles were fitted to the experimental profiles using an interactive graphic computer routine. First, the broadened theoretical profiles were shifted in wavelength to best coincide with the experimental profiles. Next, the intensity of the theoretical profile was multiplied by a scaling factor, so that the areas under the theoretical and experimental profiles were equal.

Although other fitting procedures such as a least-squares fit were tested, it was felt that area normalization maintained the most objective fitting procedure. To characterize the quality of the fit a normalized sum of the squares parameter Q was used. This Q is defined by

$$Q=\sum(y_{\text{expt}}-y_{\text{theor}})^2/\sum y_{\text{theor}}^2.$$

Here y_{expt} and y_{theor} are the experimental points and the theoretical points at the same wavelength, and the sum was over all of the digitized experimental points. In general, a fit with $Q=0.01$ is good, whereas a fit with $Q=0.1$ is poor; examples will be shown in Sec. V.

D. The idealized fitting procedure

The two major variables in determining the width of the observed emission line are n_e and n_1 (for a given l). The gross width of any line is not a unique function of n_e and n_1. The details of a line shape, e.g., the height of shoulders, may be a unique function of n_e and n_1, but it is only the coarse features that are observable. If the theory

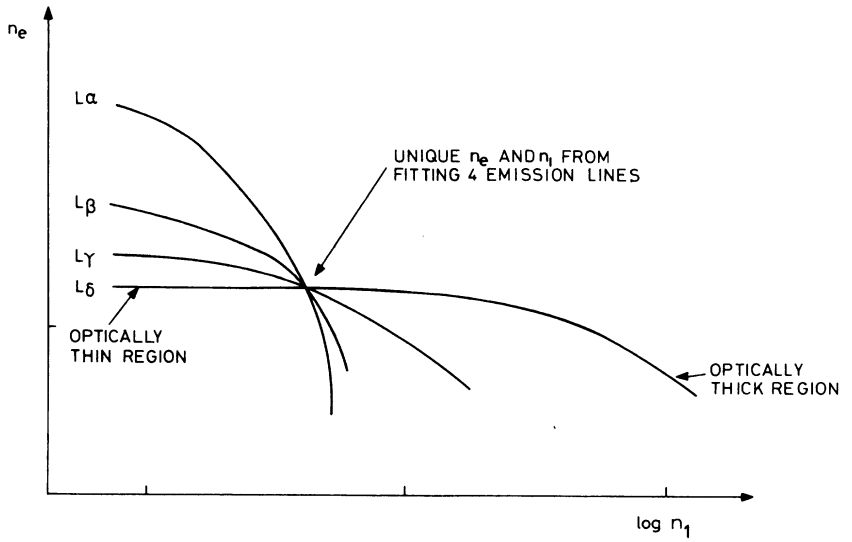

FIG. 4. The ideal lines of the best fit in n_e, n_1 parameter space of the theoretical opacity, corrected line profiles to a given set of experimental profiles.

is compared with a given experimental profile, then for a small optical depth the linewidth will be a function of n_e only; and if the line of best fit is plotted on a graph of n_e vs n_1 as in Fig. 4, it will be a horizontal line. As the line becomes optically thick, the same total theoretical width can be obtained with a smaller n_e. Thus the line of best fit curves downwards as in Fig. 4. Ideally, a line of best fit could be obtained for several transitions and they would intersect at one point in the n_e, n_1 plot, characterizing n_e and n_1 in the slab.

In fact, the line of fit is an area determined by the constraint on Q which was taken as $Q < 2\,Q_{\min}$ where $Q_{\min}$ is the quality of the best fit. Thus instead of a point in the n_e, n_1 space, an area should be defined by the common overlapping area of several transitions.

The maximum state of ionization can also be represented on the n_e, n_1 plot. If, for example, the plasma is of one element of atomic density n_a and average charge Z,

$$n_H < 0.5\, n_a = (0.5/Z) n_e ,$$

this describing an allowed region in the n_e, n_1 parameter space. Similarly, the state of ionization as determined in Sec. III B can be represented as a line on the n_e, n_1 plot.

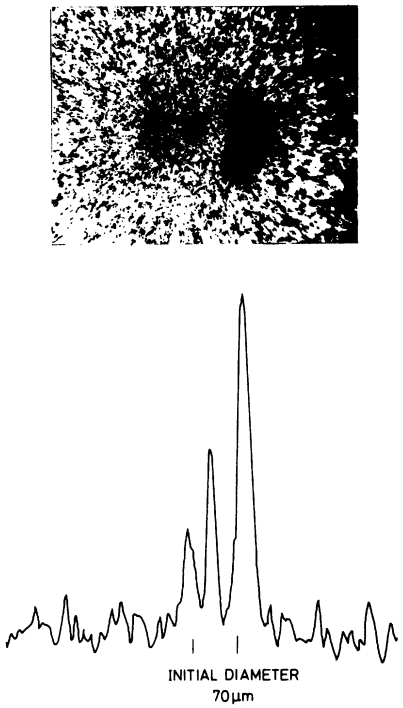

FIG. 5. The pinhole photograph and densitometer trace for shot 167.

V. COMPARISON OF THEORY AND EXPERIMENT

A. Emission from the surface plasma on a microballoon

The diagnosis of the surface region is illustrated by analyzing case I (shot 167). The target for this shot was a microballoon of diameter 70 μm with a thick coating of aluminum, preventing the underlying glass from becoming hot enough to emit in the x-ray region. The target was irradiated by 12 J of laser energy in 100 ps with one beam being 25% more intense than the other. The pinhole photograph is shown in Fig. 5. A space-resolved spectrum, with a 10-μm slit, was obtained and a densitometer tracing is shown in Fig. 6.

i. The electron temperature. The recombination continuum shown in Fig. 6 indicates from its slope a temperature of 650 ± 100 eV. As an example of shell spectra this temperature is above the average of 500 eV, but is a particularly good example for the spectral line fitting because the $L\delta$ line is well above the continuum level.

The measured ratio of the Al^{12+} $L\gamma$ to Al^{11+} $1\,^1S_0 - 4\,^1P_1$ lines was 0.54. From Eq. (3) this implies a ratio of

$$n(Al^{13+})/n(Al^{12+}) = 0.2 .$$

Using the optically thin CRE model (Fig. 7) at a density of 10^{22} cm^{-3}, the temperature required for this ratio is 500 eV. As described in Sec. III B, the coronal model predicts that 35% of the aluminum atoms will be in the hydrogenic state of ionization.

ii. The size of the emitting region. A microdensitometer scan of the pinhole photograph (Fig. 5) shows that the full width at half maximum (FWHM) of the x-ray emitting region in a direction normal to the laser beam axis is 45 μm. If this were the source size for spectral lines the instrument width would be 5 mÅ. However, the dielectronic satellite lines of Al^{12+} $1\,^1S_0 - 2\,^1P_1$ had a measured spectral width of 2.5 mÅ. As the source size for lines could be different from the spectrally integrated source size on the pinhole camera, the value of 2.5 mÅ is taken as more accurate than 5 mÅ. For the opacity-broadening length [Eq. (5)] the value of 45 μm is used. However, this may be an overestimate if the emission comes from a curved thin shell of plasma.

The continuum intensity gives a value of $n_e^2 V$ of 6.6×10^{36} cm^{-3}. Integrating the continuum and assuming isotropy shows that 9.5 mJ is emitted in the hydrogenlike recombination continuum from the more intense side of Fig. 5. The corresponding figure for the resonance transitions of AlXII and AlXIII is 3 mJ, again assuming isotropy. Note that for the optically thick lines, this assumption will be invalid.

iii. Line broadening. The AlXIII Lyman lines

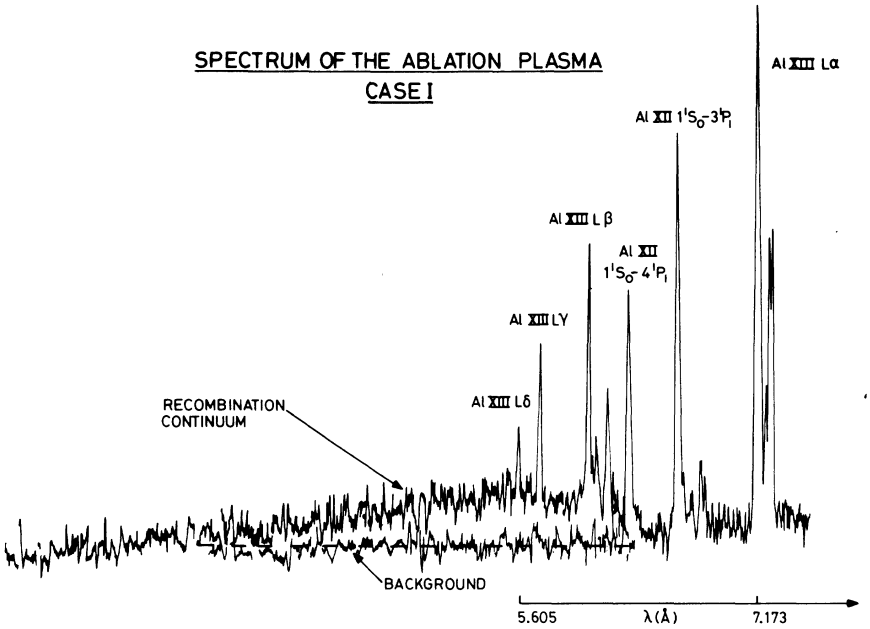

FIG. 6. A coarse microdensitometer tracing of the more intense shell emission from shot 167.

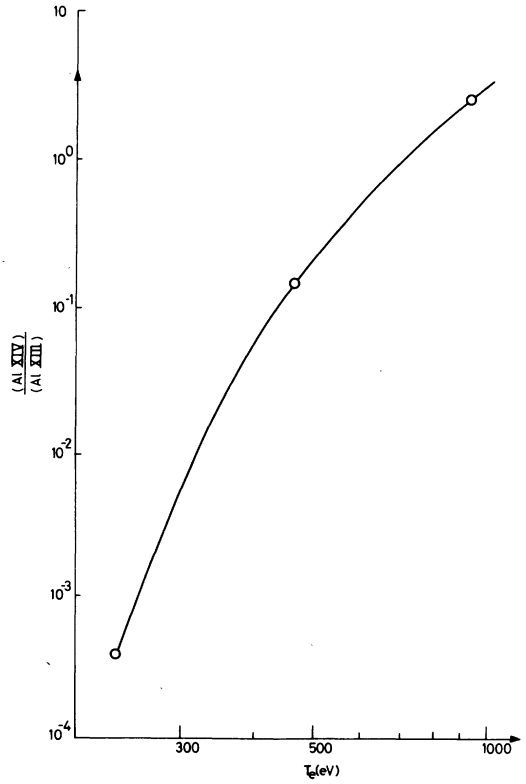

FIG. 7. The ratio of bare to hydrogenic species of aluminum as a function of T_e from the collisional radiative equilibrium model.

are now compared with the theoretical profiles. All comparisons are with area normalization and an instrument width of 2.5 mÅ. Figure 8 shows one particular fit for the $L\delta$ line, where the quality of the fit is very good, i.e., $Q = 0.007$. Note that the linewidth is much greater than the instrument width. In Fig. 9 one particular fit is shown for the $L\gamma$ transitions. The characteristic central peak of a γ profile is suppressed by opacity and instru-

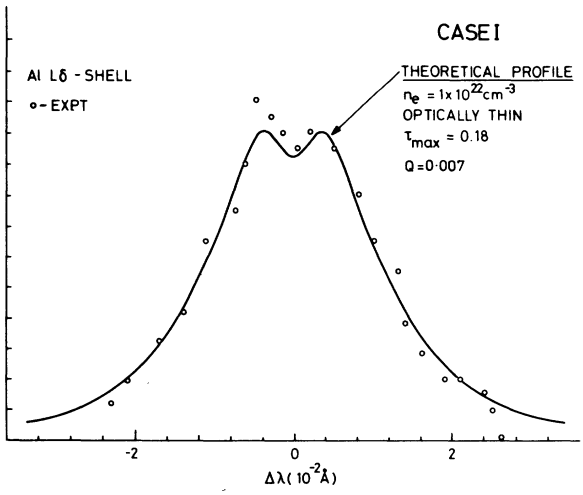

FIG. 8. A fit of the Al XIII $L\delta$ surface plasma emission to an optically thin theoretical profile. The quality of fit is good, with $Q = 0.007$.

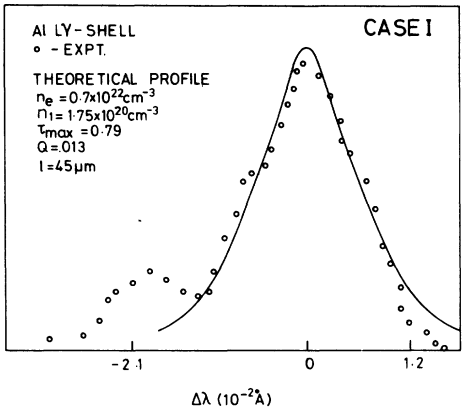

FIG. 9. A fit of the Al XIII $L\gamma$ surface plasma emission to a theoretical profile.

ment broadening. The quality of $L\beta$ fits are worse with $Q_{min} = 0.017$ for optically thin fits, because the observed profile does not have the central dip in it predicted by theory.

The region in n_e, n_1 space where the δ, γ, and β lines fit is shown in Fig. 10. The error bars shown extend all along the lines of best fit and indicate the FWHM of $1/Q$. Although the δ, γ, and β lines are consistent, the α line is markedly too narrow, using standard theory, and is off the scale of Fig. 10. The full theory, shown in Fig. 10, gives intrinsically wider profiles, thus improving but not removing the inconsistency of the α line with the β, γ, and δ lines. It can also be seen by inspection of Fig. 10 that simply considering the Ly γ, Ly δ lines as optically thin would be marginally correct—for here we see that both lines show the effects of opacity in the region where self-consistency is found, i.e., for values $n_1 \gtrsim 3\times10^{20}$ cm^{-3}. The peak optical depth of the α line is 150 and therefore the simple opacity broadening is inadequate because non-LTE effects become important as discussed in Sec. VI.

An additional constraint on the allowed region in the n_e, n_1 parameter space is derived from the state of ionization. As 35% of the Al atoms are hydrogenic, and the average charge is approximately 12, then from quasineutrality

$$n_e = (12/0.35)n_1 \cong 30n_1 .$$

The region $n_e = 0.03n_1$ is shown in Fig. 10 together with the "forbidden region" for which more than 50% of the Al atoms are hydrogenlike. These lines, together with the β, γ, and δ areas of best fit, give $n_e = (1.0\pm0.3)\times10^{22}$ cm^{-3}.

B. The compressed glass plasma

Case II (shot 209) is a good example of the diagnosis of the properties of the compressed glass in the core. The microballoon target for this shot was 66 μm in diameter, with a 0.75-μm wall thickness and was filled with approximately 0.3 bar of argon. It was imploded by 22 J of laser energy in 100 ps. A part of the space-resolved spectrum is shown in Fig. 11. The core is distinct from the

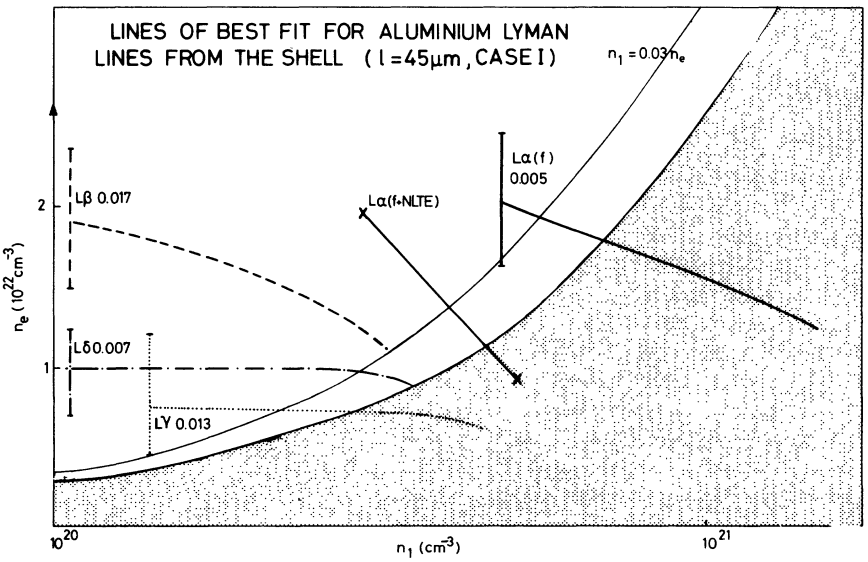

FIG. 10. The lines of best fit in the n_e, n_1 parameter space for the surface plasma emission. The error bars run all along the lines of best fit indicating the region where $Q < 2.0_{min}$. The lines of best fit for $L\alpha$ are shown for the full theory $L\alpha(f)$ with LTE opacity broadening and with non-LTE (NLTE) opacity broandening. The shaded region is forbidden whatever the ionization equilibrium model. The state of ionization line using the coronal model is also shown.

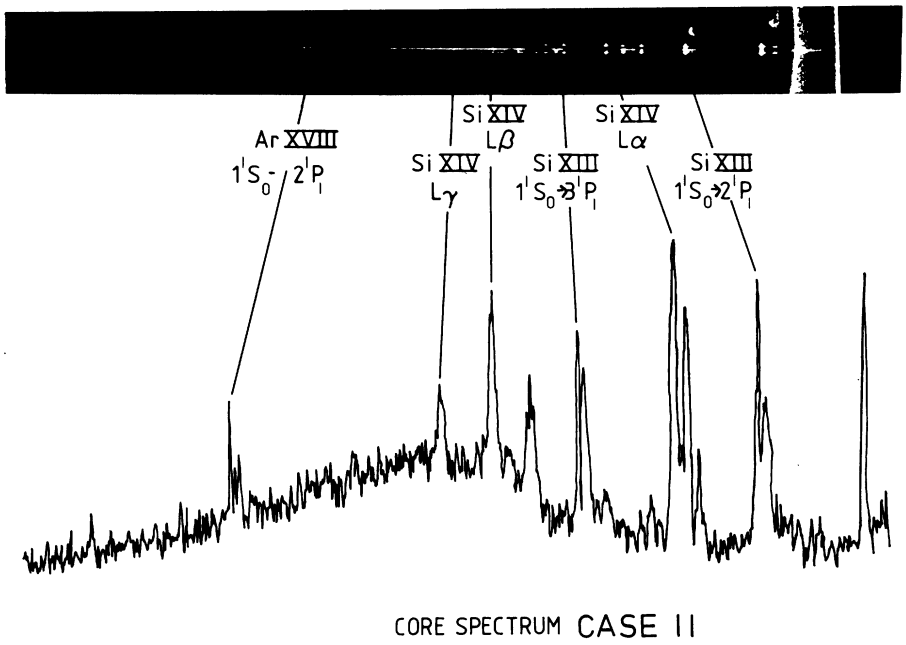

FIG. 11. Part of the space-resolved spectra obtained on shot 209 and a densitometer tracing of the core spectrum.

x-ray-emitting shell regions and shows emission of AlXII, AlXIII, SiXIII, SiXIV, and ArXVII lines and a Si recombination continuum.

i. The electron temperature. The spectral intensity of the recombination continuum $\epsilon_\nu(\nu)$ is shown in Fig. 12. In the range $2.5 < h\nu < 3.2$ keV, the slope indicates $T_e = 430 \pm 40$ eV. Using the measured line ratio,

$$\frac{I(L_\gamma(\mathrm{Si}^{14+}))}{I(1\,{}^1S_0\text{-}4\,{}^1P_1(\mathrm{Si}^{13+}))} = 0.45 \pm 0.09\,.$$

From Eq. (3) this implies

$$n_B/n_H = 0.17 \pm 0.03\,.$$

Optically thin CRE requires $T_e = 600 \pm 20$ eV for this ratio. As before, the coronal model implies that 30% of the silicon atoms are Si XIV.

ii. The core size. By tracing the silicon recombination continuum in the spatial direction, the diameter of the silicon-emitting region was found to be 22 ± 2 μm. The intensity of the Si recombination continuum step implies that $n_e^2 V = 3.5 \times 10^{37}$ cm^{-3} assuming an emission time of 50 ps.[14] Because of the low filling pressure of argon, most of the core is glass and so the volume of Si emission is taken as a sphere of diameter 22 μm. The electron density is then estimated to be 8×10^{22} cm^{-3}, although the error bars on this will be determined by the error in V.

iii. Line broadening. By comparing the spectral profiles of the SiXIV $L\alpha$, $L\beta$, and $L\gamma$ lines, the lines of best fit in n_e, n_1 parameter space were obtained, and are shown in Fig. 13. As before, the $L\alpha$ fits using standard theory do not agree with $L\beta$ and $L\gamma$, but the full theory applied to the $L\alpha$ line removes the discrepancy. A fit of the Si $L\beta$ profile to the standard theory is shown in Fig. 14. Figure

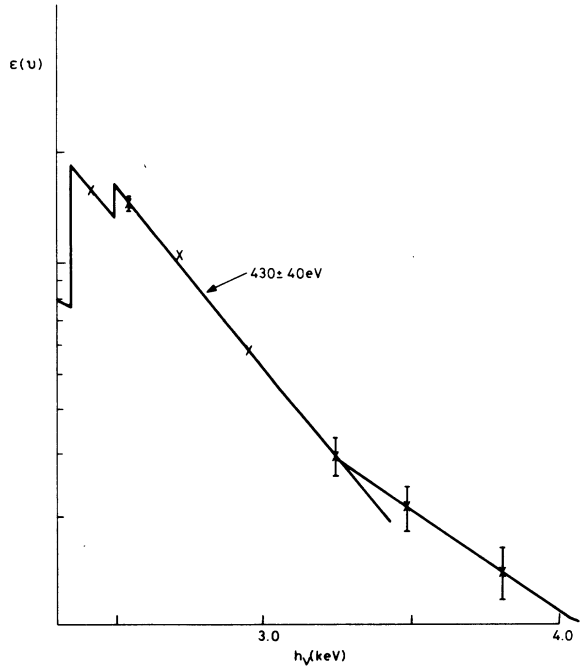

FIG. 12. The time-integrated spectral intensity of the Si XIII and Si XIV recombination continuum on shot 209.

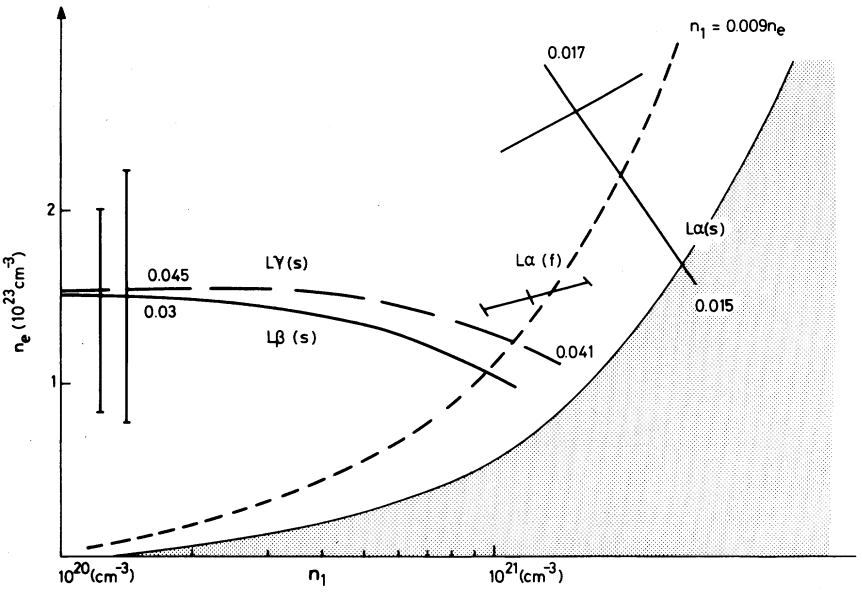

FIG. 13. The lines of best fit in the n_e, n_1 parameter space for the silicon Lyman emission lines from the core. The fits of the $L\alpha$ line using standard $L\alpha(s)$ and full $L\alpha(f)$ calculations of the optically thin profiles are shown. The shaded area is the forbidden region.

14 illustrates the fit with the parameter Q as low as obtainable for any n_e, n_1 combination; increasing the opacity n_1 does not yield better fits. This is presumably due to the spatial and temporal integrations changing the detailed shape of the experimental profile in an unknown way. The quality of the β and γ fits is poor, but this is because the fine detail of the theory profiles, the central dip of the $L\beta$ and the central peak of $L\gamma$, are not seen experimentally.

The state of ionization line is also shown in Fig. 13, together with the forbidden region. Assuming that the core is SiO_2 and that 30% of the Si is Si XIV, then $n_1 = 0.009n_e$. The allowed region is $n_1 < 0.015n_e$. It can be seen that a consistent fit can be obtained only with the full theory and then $n_e = (1.5 + 0.4 - 0.2) \times 10^{23}$ cm^{-3}, $n_1 = (1.2 \pm 0.4) \times 10^{21}$ cm^{-3}.

The Si XIII series can also be studied. The Si XIII $1\,^1S_0$-$3\,^1P_1$ profile was not studied consistently, but is particularly interesting and is shown in Fig. 15. A very high electron density is needed to fit this line. A high opacity will not give a good fit because this has the effect of equalizing the

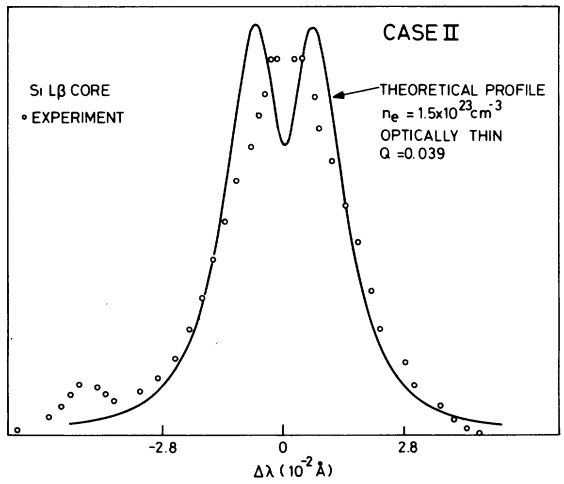

FIG. 14. A fit of the Si XIV $L\beta$ core emission on shot 209 to an optically thin theoretical profile.

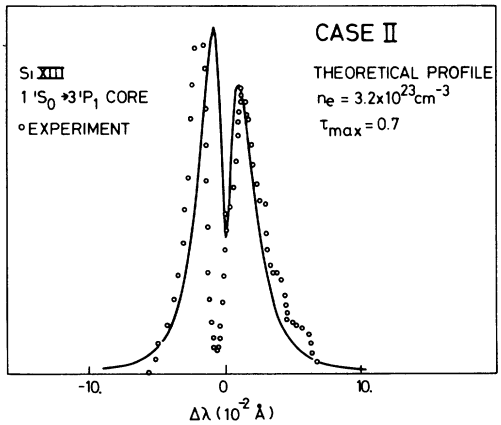

FIG. 15. A fit of the heliumlike Si $1\,^1S_0$-$3\,^1P_1$ line on shot 209 to a theoretical profile. The large dip at the center of the experimental profile is probably due to reabsorption by cool low density Si XIII in the outer region.

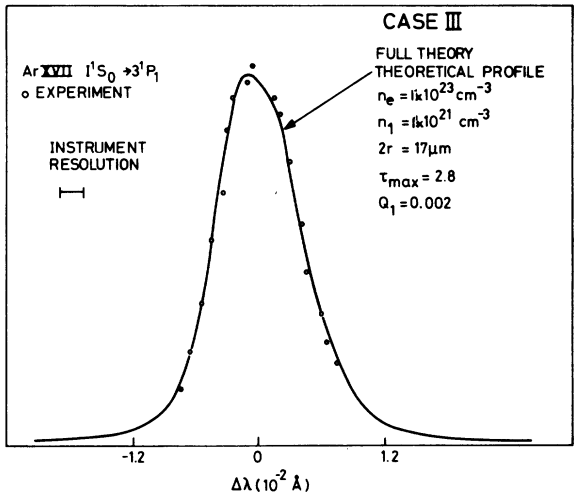

FIG. 16. A fit of the heliumlike argon 1^1S_0-3^1P_1 lines on shot 209 to a theoretical profile using the full theory.

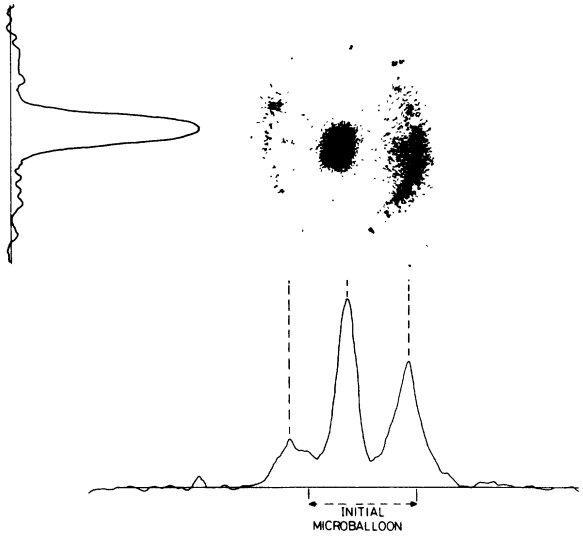

FIG. 17. The x-ray pinhole photograph and densitometer trace on shot 242.

two peaks of the theoretical profile. The dip in the center of the experimental profile is much larger than in the theoretical profile and is probably due to absorption by cool low-density Si XIII in the outer region of the plasma.

One further completely novel aspect of this shot is the presence of broadened argon lines. The spectrum showed Ar XVII 1^1S_0-2^1P_1 and Ar XVII 1^1S_0-3^1P_1 lines, both of which are broadened beyond the instrument width. A fit to the theory for the latter line is shown in Fig. 16.

C. The compressed gas plasma

The x-ray diagnosis of the compressed gas plasma can be illustrated by shot 242. The target was a 102-μm-diameter, 0.58-μm-wall-thickness microballoon filled with 2 bar of Ne. It was imploded by a 16 J, 100-ps laser pulse (8 J per beam). The pinhole photograph is shown in Fig. 17. A space-integrated spectrum was recorded with a thallium-acid-phthalate (Tl.A.P.) crystal spectrometer and

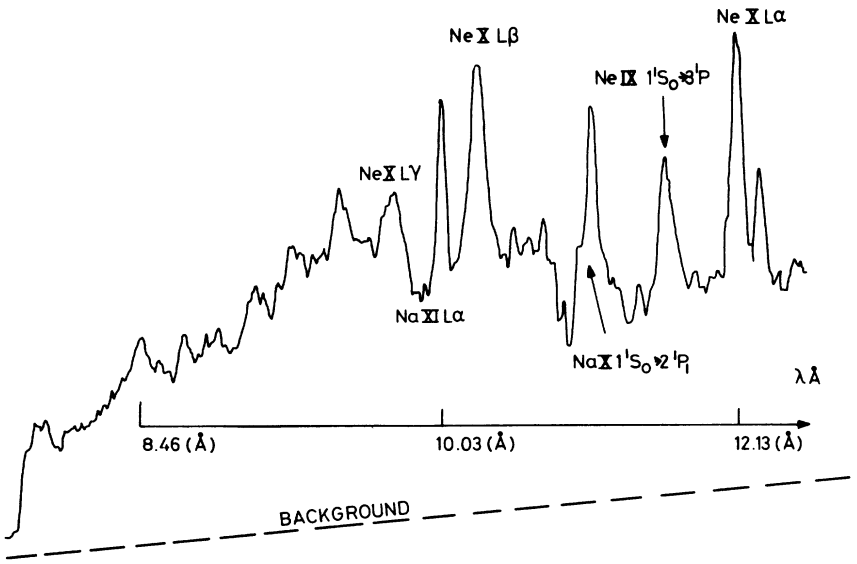

SPACE INTEGRATED SPECTRUM CASE III

FIG. 18. The space-integrated Tl.A.P. spectrum from shot 242.

a space-resolved spectrum was recorded with a pentaery thritol (PET) crystal spectrometer. A tracing from the Tl.A.P. crystal spectrometer is shown in Fig. 18. This figure shows Ne XI and Ne X lines together with Na lines from the glass. The space-resolved spectrometer shows very little Si line emission from the core, but does show strong core continuum emission from the Ne IX and Ne X recombination continuum.

i. The electron temperature. From the Ne X and Ne IX recombination continuum slope it was found that $T_e = 300 \pm 50$ eV. Using the measured line intensity ratio,

$$\frac{I(L\beta(\mathrm{Ne}^{9+}))}{I(1\,^1S_0 \rightarrow 3\,^1P_1(\mathrm{Ne}^{8+}))} = 1.50\,,$$

then from Eq. (3)

$$n_B/n_H = 1.5\,.$$

Optically thin CRE requires an electron temperature of 370 eV to achieve this state of ionization. As before, the coronal model implies that 50% of the Ne atoms would be hydrogenic.

ii. The core size. On this shot, it is evident from the pinhole photograph (Fig. 17) that the core is not spherical. This is a result of the large size of the microballoon and the double-beam irradiation. From the pinhole photograph the larger FWHM intensity of the microballoon is 28 ± 2 μm. The transverse (smaller) size of the core is best obtained from the space-resolved PET spectrometer and is 12 ± 1 μm. The intensity of the neon recombination step implies $n_e^2 V$ is 2×10^{36} cm^{-3}, assuming an emission time of 80 ps. With the above core dimensions this gives $n_e \sim 2 \times 10^{22}$ cm^{-3}.

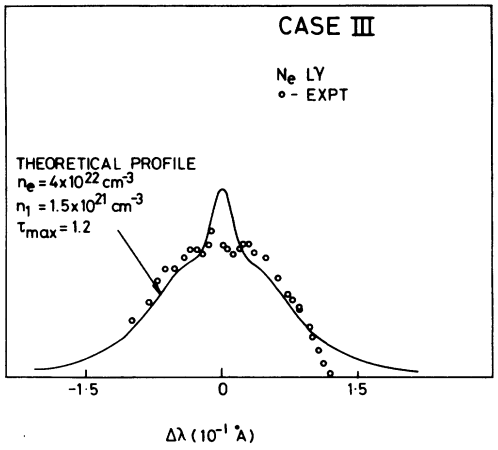

FIG. 19. A fit of the NeX $L\gamma$ line on shot 242 to a theoretical profile.

iii. Line broadening. The Ne X $L\alpha$, $L\beta$, and $L\gamma$ lines were fitted to the theoretical profiles as described in Sec. IV. Good fits with $Q \sim 0.01$ were obtained for the $L\alpha$ and $L\beta$ lines. A $L\gamma$ line fit is shown in Fig. 19. As usual, the central feature of the theoretical profile is not seen experimentally, resulting in a poor quality fit $Q = 0.036$. The lines of best fit for all three lines are shown in Fig. 20. The effect of using the full theory for the line broadening is not very pronounced in this case because Z is lower. Also shown is the region $n_1 > 0.05 n_e$, which represents 50% of the neon atoms being Ne X, and is therefore the forbidden region. From the intersection of the $L\beta$, $L\alpha$ and the state of ionization lines $n_e = (2.8 \pm 0.5) \times 10^{22}$ cm^{-3} and $n_1 = (1.4 \pm 0.4) \times 10^{21}$ cm^{-3}.

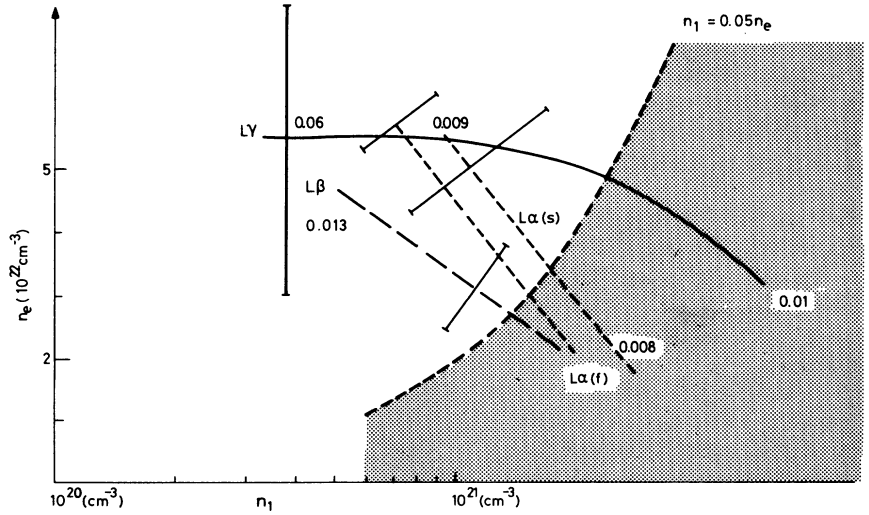

FIG. 20. The lines of best fit for shot 242. Fits for the $L\alpha$ line are shown with the full and standard theories. The edge of the forbidden region (shaded) is also shown, as is the state of ionization line.

TABLE II. Parameters of case studies.

Description	Surface plasma	Compressed glass	Compressed gas
Shot	167	209	242
Element	Al	Si	Ne
Section of this paper	Sec. V A	Sec. V B	Sec. V C
Continuum temperature (eV)	650 ± 100	430 ± 40	300 ± 50
Line ratio temperature (eV)	500 ± 50	600 ± 20	370 ± 30
Hydrogenic fraction	0.35	0.30	0.50
Source size (μm)	45 ± 5	22 ± 2	28 ± 2, 12 ± 1
Lyman lines used	$\alpha, \beta, \gamma, \delta$	α, β, γ	α, β, γ
$n_e \times 10^{-22}$ cm^{-3}	1 ± 0.3	$15\{^{+4}_{-2}$	2.8 ± 0.5
$n_1 \times 10^{-20}$ cm^{-3}	4 ± 1	12 ± 4	14 ± 4
$a = r_0/\lambda_D$ (see text)	0.15	0.29	0.23

The above core dimension gives a volume of 4×10^{-9} cm^{-3}. If $n_e = 2.8 \times 10^{22}$ cm^{-3} and with $Z = 9$, then the number of neon atoms in the hot core is 1.2×10^{13} compared with the initial 2.8×10^{13} neon atoms. A factor-of-two discrepancy is probably not significant in light of the accuracy of the determination of the emitting volume.

VI. DISCUSSION AND REVIEW

A. Optically thin profiles

The ion microfields are calculated in terms of an expansion parameter a, the ratio of the interparticle spacing r_0 to the Debye length λ_D. Here a is sufficiently small so that the expansion is well defined (see Table II).

The full theory with the dynamic broadening, i.e., ion and electron collisional contributions included, has been verified at lower densities.[27] Furthermore, the theory reproduces the standard results of Kepple and Griem[29] to better than 5% in the limit of static ions and no Z-dependent shifts and widths.

Effects due to thermal levels of plasma waves are included in this theory. However, as shown in Ref. 28 the extremely large Landau damping in these plasmas makes wave effects negligible in these plasmas if they are in equilibrium and can be described as thermal.

There are other considerations, such as the applicability of the random-phase approximation (RPA), and the importance of nonideal effects on the plasma dielectric function.[31] However, because of the small values of a, i.e., less than 0.31, found in these plasmas these effects are unimportant. Finally, the possibility of a nonideal-type shielding cloud has been proposed.[33] This is an effect of the electrons in the Debye shielding cloud of ions; however, the effect proposed is indeed included in the full RPA description of the plasma, and hence its existence as a distinct entity and its eventual inclusion into the line profile by convolution are unnecessary.

Thus these optically thin profiles are considered accurate to better than 20% in all regions of the line profile, and if the central portion of the Lyman α-like transitions is excluded the estimate improves.

B. Assumption of homogeneity and time invariance

To assume anything but homogeneity would be artificial with our present poor state of knowledge. Furthermore, even if the plasma inhomogeneity were known, there is at present no viable method of describing the radiation transfer in an inhomogeneous time-varying plasma.

Measurements with time-resolved spectroscopy have recently been made[14] and the Ne line emission in the core is short lived (<100 ps). The shell emission on the other hand persists for up to 400 ps, i.e., is much longer than the 100-ps laser pulse; it is considerably weaker and appears spectrally narrower after the laser pulse than during the laser pulse. The effect of time integration is therefore to make the profile appear slightly narrower than it is during the laser pulse.

C. Radiation transfer

Given the assumption of an homogeneous plasma, our simple prescription for the radiation transport can still be incomplete because of non-LTE

effects.[30, 32, 34] These effects are characterized by the parameter ϵ' which is the ratio of the collisional deexcitation rate to the spontaneous radiative decay rate. When $\epsilon' \gg 1$ the source function will be collisional, i.e., LTE. For non-LTE effects, an $\epsilon' < 1$ is a necessary although not sufficient condition; additionally, a high optical depth is required. The $L\alpha$ transition in this study will be most affected having $0.2 < \epsilon' < 0.4$ and a large optical depth. The optical depth of the higher-order series members is much lower and hence non-LTE effects are not important.

If incoherent transfer of radiation is included, then photons can diffuse in frequency space as well as real space. Diffusion in frequency space will occur until a frequency is reached for which there is a high probability of escape.[30, 32, 34]

To gain insight into the importance of these extra effects, the analytic formulas of Wilson[35] for a two-level atom have been implemented. These constitute a simple Eddington approximation for non-LTE transport of the flux. In our cases the effects of the redistribution due to frequency diffusion in the line are relevant for the shell plasma where higher optical depths are found. The frequency diffusion creates a trough at the center of the line but does not appreciably change the half width of the line. However, when the redistributed line profile is convolved with the instrument function the peak can be reduced by filling in the trough and thus broadening the line profile. This effect is significant for the shell plasma since the instrument width is a non-negligible fraction of the linewidth. As an example of the result of this broadening (non-LTE frequency redistribution plus instrument broadening), the Al XIII $L\alpha$ line from the shell was fitted (Sec. V A). As shown in Fig. 21 the trough at the line center is still evident after instrument broadening but the overall broadening is substantially larger than for the LTE transfer case. When these fits are shown on the n_e, n_1 plot Fig. 10, it is seen that the inconsistency between the widths of the $L\alpha$ and the $L\beta$, $L\gamma$, and $L\delta$ lines is removed.

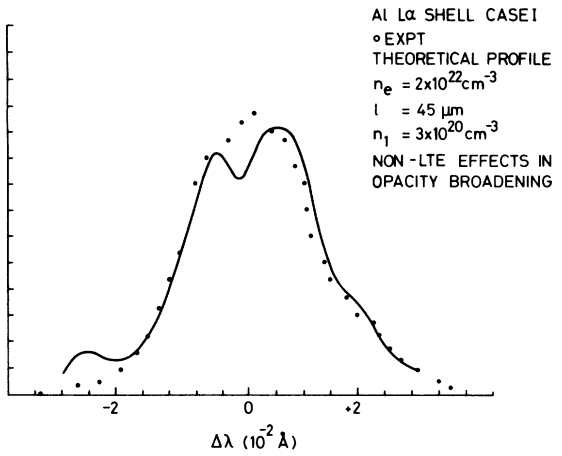

FIG. 21. A fit of the Al XIII $L\gamma$ line to the full theory using the non-LTE opacity broadening. Even after instrument broadening the dip at line center due to the non-LTE broadening is still apparent.

D. Doppler effects

The inclusion of Doppler shifts due to plasma motion will not be of any significance for the core plasma because of the low velocities associated with the core and the fact that at the peak electron density, and thus emissivity, the velocity of the core is most likely minimized. For the shell it is reasonable that the velocity of the x-ray-emitting region, which is at a higher density than the critical density, should be less than 10^7 cm s^{-1}, the velocity of the critical density surface as measured by time-resolved second-harmonic emission.[9] However, as observations here are approximately normal to the laser beam, the Doppler shift will be considerably less than $\lambda v/c = 2$ mÅ, the shift for 10^7 cm s^{-1} velocity. Therefore, Doppler shifts and broadening are negligible.

E. Dielectronic satellites

In shot 209 (subsection *iii* of Sec. V B) it was pointed out that the intensity of the well-resolved dielectronic satellites was high. However, there are satellites due to transitions of the type $1s3l^- - 2l3l^-$ which are not well resolved from the fundamental Si XIV $L\alpha$ transition. Although usually much less intense than the main transition, the relative intensities of such satellites can be increased because of opacity effects. Such an effect would apparently broaden the main transition.

F. Summary and conclusions

It has been shown how information on the plasma density temperature and optical depth can be obtained with x-ray instruments. A self-consistent fit for all the lines of a series has been demonstrated for the first time. Argon emission has been observed and analyzed for the first time, and electron densities in excess of 10^{23} cm^{-3} have been measured spectroscopically for the first time. Further heliumlike lines have been used for the first time to corroborate the hydrogenlike line analysis.

In the analysis of this data it has been shown that one cannot obtain a single value of electron density from the optically thin transitions and a unique optical depth from the lower series mem-

ber. This is because of the following.

(1) The quality of the data leads to fits over a wide range of parameters, even for the optically thin lines.

(2) For lines with medium and high optical depth, fits depend on both n_e and n_1, thus necessitating an area of fit in the n_e, n_1 parameter space.

To obtain consistency between all the transitions of a series, it has been shown that additional physical phenomena must be included. These are as follows:

(1) Effects arising from the Z-dependent shifts and widths which increase the linewidth;

(2) non-LTE radiation transfer which is needed to describe the opacity broadening of low-series members.

[1]S. L. Mandel'shtam, P. P. Pashinim, A. M. Prokhorov, Yu. P. Raizer, and N. K. Sukhodrev, Zh. Eksp. Teor. Fiz. 49, 127 (1965) [Sov. Phys.—JETP 22, 91 (1966)].

[2]D. D. Burgess, B. C. Fawcett, and N. J. Peacock, Proc. Phys. Soc. London 92, 805 (1967).

[3]S. M. Mead, R. E. Kidder, J. E. Swain, F. Rainer, and J. Petrazzi, Appl. Opt. 11, 345 (1972).

[4]G. Charatis *et al.*, *Plasma Physics and Controlled Nuclear Fusion Research* (IAEA, Vienna, 1975), Vol. 2, p. 317.

[5]V. A. Boiko, S. A. Pikiiz, and A. Ya. Faenov, Kvant. Elektron. (Moscow) 2, 1216 (1975) [Sov. J. Quant. Elec. 5, 658 (1975)].

[6]E. Valeo, H. R. Griem, J. Thomson, and D. Bailey, Lawrence Livermore Laboratory Report No. 50021-73, 327, 1976 (unpublished).

[7]L. M. Richards *et al.*, Bull. Am. Phys. Soc. 21, 1141 (1976).

[8]B. Yaakobi and A. Nee, Phys. Rev. Lett. 36, 1077 (1976).

[9]J. M. Auerbach, Lawrence Livermore Laboratory Report No. 135 Annual Report 1976, p. 5 (unpublished).

[10]B. Yaakobi, D. Steel, S. E. Thorsos, A. Hauer, and B. Perry, Phys. Rev. Lett. 39, 1526 (1977).

[11]M. H. Key *et al.*, Eleventh European Conference on Laser Interaction with Matter, Rutherford Laboratory Report No. RL 77 122/B, 1977 (unpublished).

[12]B. Yaakobi *et al.*, Laboratory for Laser Energetics Report No. 74, 1978 (unpublished).

[13]M. H. Key *et al.*, Topical meeting on Inertial Confinement Fusion, San Diego, U.S.A., Rutherford Laboratory Report No. RL 78 020, 1978 (unpublished).

[14]Annual Report to the Laser Facility Committee Rutherford Laboratory, Report No. RL 78 039, 1978 (unpublished).

[15]M. H. Key, J. G. Lunney, J. M. Ward, R. G. Evans, and P. T. Rumsby, J. Phys. B 12, L213 (1979).

[16]K. B. Mitchell, D. B. Van Husteyn, C. H. McCall, P. Lee, and H. R. Griem, Phys. Rev. Lett. 42, 232 (1979).

[17]B. Yaakobi *et al.*, Phys. Rev. 19, 1247 (1979).

[18]J. M. Auerbach *et al.*, J. Appl. Phys. 50, 5478 (1979).

[19]M. H. Key, J. G. Lunney, J. D. Kilkenny, and R. W. Lee, Appl. Phys. Lett. 36, 269 (1980).

[20]M. C. Hobby and N. J. Peacock, J. Phys. E 6, B4 (1973).

[21]K. D. Evans *et al.*, X-Ray Spectrom. 6, 132 (1977); G. Elwert, Z. Naturforsch. 9A, 637 (1954).

[22]H. R. Griem, *Plasma Spectroscopy* (McGraw-Hill, New York, 1964).

[23]D. R. Bates, A. E. Kingston, and R. W. P. McWhirter, Proc. R. Soc. London Ser. A 267, 297 (1962).

[24]D. R. Bates, A. E. Kingston, and R. W. P. McWhirter, Proc. R. Soc. London Ser. A 270, 155 (1962).

[25]C. Jordan, Mon. Not. R. Astron. Soc. 142, 501 (1969).

[26]R. W. Lee, J. Phys. B 12, 1129 (1979).

[27]R. W. Lee, J. Phys. B 12, 1144 (1979).

[28]R. W. Lee, Phys. Lett. 71A, 224 (1979).

[29]P. C. Kepple and H. R. Griem, NRL Memorandum Report No. 3382, Naval Research Laboratories, Washington, D.C., 1976 (unpublished).

[30]D. Mihalas, *Stellar Atmospheres* (Freeman, San Francisco, 1978).

[31]P. B. Kunasz and D. G. Hummer, Mon. Not. R. Astron. Soc. 166, 19 (1974).

[32]I. Cook, Plasma Phys. 20, 73 (1970).

[33]H. R. Griem, Phys. Rev. A 214 (1973).

[34]E. H. Averett and D. G. Hummer, Mon. Not. R. Astron. Soc. 130, 295 (1965).

[35]R. N. Wilson, Mission Research Corporation Report No. MRC-R-11, 1972 (unpublished).